Nonlinear Analysis of Arches: A Comparison Among Three Recent Methodologies Applied to a Multi-ring Model

Gandolfi Alessandro[1(✉)], Hua Yiwei[1], Pingaro Natalia[1,2], and Milani Gabriele[1]

[1] Department of Architecture, Built Environment and Construction Engineering, Politecnico di Milano, Piazza Leonardo da Vinci 32, Milan, Italy
alessandro.gandolfi@polimi.it

[2] European Centre for Training and Research in Earthquake Engineering (EUCENTRE Foundation), 27100 Pavia, Italy

Abstract. The structural assessment of masonry arches is challenging due to their heterogeneous composition and highly nonlinear response. This is particularly relevant in for multi-ring arches where inter-ring joints and interlocking govern the sliding, hinging, and ring separation mechanisms that simplified homogeneous approaches cannot capture. This paper compares three recent heterogeneous strategies for the nonlinear analysis of a representative multi-ring masonry arch. First, a heterogeneous Limit Analysis approach with a non-associated flow rule is employed to estimate collapse loads while avoiding artificial dilatancy effects. Second, an automated Ruled Explicit Meshing (REM) workflow is used to generate Elastic Body and Spring Models compatible with commercial FE software. Starting from a simplified geometric input, the routine produces block–interface representations with limited user intervention, reducing modelling time and modelling inconsistencies. The third approach, the FEMANOLA code, is adopted to simulate the full nonlinear response, including damage evolution and interaction between failure modes, though requiring deeper calibration. The comparison highlights the advantages and limitations of each approach in terms of ultimate capacity, damage evolution, computational effort, and practical applicability.

Keywords: Multi-ring arches · Heterogeneous Modelling · Elastic Body and Spring Method (EBSM) · Ruled Explicit Meshing (REM) · Limit Analysis (LA) · FEMANOLA

1 Introduction

The structural assessment of masonry arches is inherently complex due to the heterogeneous nature of the material and its nonlinear and asymmetric behaviour [1, 2]. These challenges are further amplified in multi-ring arches, even though they constitute a small fraction of existing masonry structures. The presence of ring interfaces introduces additional planes of weakness, making ring separation, sliding, and interlocking effects dominant mechanisms governing the structural response [3].

© The Author(s), under exclusive license to Springer Nature Switzerland AG 2027
O. Gervasi et al. (Eds.): ICCSA 2026 Workshops, LNCS 16758, pp. 581–599, 2027.
https://doi.org/10.1007/978-3-032-30497-1_35

Experimental and numerical studies proved that the mechanics of masonry structures is strongly affected by geometry and unit arrangement [4–6]. In particular, multi-ring arches exhibit significantly different behaviour compared to single-ring ones, with failure often controlled by ring sliding and separation rather than purely rotational mechanisms [7]. Such mechanisms are controlled by ring staggering and blocks interlocking. Therefore, simplified homogeneous approaches may lead to inaccurate predictions, often overestimating the structural capacity by neglecting the discrete nature of the rings and their interaction.

To address these issues, comparable modelling strategies can be found in the literature [8–10]. Among them, three approaches are considered in this work and treated as complementary tools for the assessment of masonry arches.

A first approach is represented by heterogeneous Limit Analysis formulations, where masonry is idealised as an assemblage of rigid blocks connected by frictional interfaces. This method provides direct estimation of collapse loads and mechanisms with relatively low computational cost [11–13]. However, when non-associated flow rules are introduced to better represent frictional behaviour, the problem becomes non-linear and non-convex, leading to potential non-uniqueness of the solution and increased computational complexity.

The second approach consists of heterogeneous Finite Element (FE) modelling based on block–interface representations. Within this framework, the REM (Ruled Explicit Meshing) procedure enables the automatic generation of models starting from simplified geometric inputs. Compared to previous versions [14, 15], this strategy significantly reduces preprocessing effort and user dependency, while maintaining the ability to capture localised damage. Nevertheless, the accuracy of the results still depends on mesh assumptions and interface idealisations, and convergence issues typical of nonlinear FE analyses may arise.

Finally, FEMANOLA code represents a dedicated FE-based tool specifically developed for masonry structures. By adopting an explicit iterative strategy with progressive stiffness degradation at Gauss points, it is capable of reproducing complex nonlinear phenomena such as crack initiation, propagation, and failure modes combination. This enables a detailed description of the structural behaviour with a computational cost reduced by approximately 90% compared to REM, although it requires a more careful calibration of the mechanical parameters.

In this context, the present work proposes an automated REM-based workflow and evaluates its performance through a comparative analysis with heterogeneous Limit Analysis and FEMANOLA. The objective is to highlight the potentialities and limitations of each method when applied to multi-ring masonry arches, providing a consistent framework for their combined use in structural assessment.

1.1 The Case Study Analysed

The effectiveness of the three methodologies is demonstrated through one methodological benchmark. Although the geometry is inspired by an existing pedestrian bridge arch, the heterogeneous model and the boundary conditions are intentionally idealised to provide a repeatable comparison among the three numerical approaches. The arch in Fig. 1 spans 8271 mm, has a radial thickness of 930 mm and an out of plane depth of

660 mm. The aim is not to provide a full validation against an experimental campaign, but to compare the predictions of three independently developed methodologies under the same geometric, mechanical and loading assumptions.

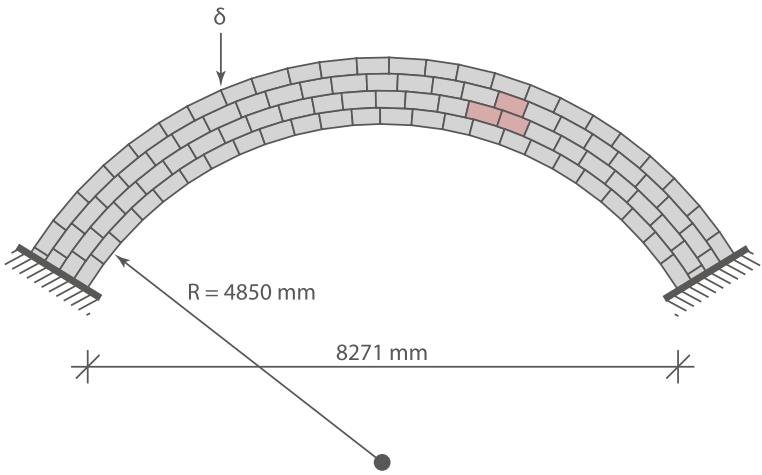

Fig. 1. Geometrical description of the multi-ring arch analysed

2 Heterogeneous Limit Analysis

In this section, a Limit Analysis (LA) formulation is used to compute the collapse load of the abovementioned structure. The arch bricks are simulated through rigid elements, with the plasticity reduced only at the interfaces. The interface constitutive model follows the classic Mohr-Coulomb friction with tension cutoff, considering both associated and non-associated flow rules. The LA formulation is constructed from a kinematic view.

2.1 Recall of Associated Limit Analysis Formulation

Determining the kinematics of the rigid units is quite straightforward. The velocity field of the rigid element with arbitrary polygonal shapes can be expressed as in Eq. (1). $\mathbf{u}^i$ contains the three rigid-body velocity components in 2D, and the mapping matrix $\mathbf{H}_{\mathcal{R}}(\mathbf{r})$ correspondingly collects in columns three 2D rigid-body basis modes (given in Eq. (2)).

$$\mathbf{u}^i(\mathbf{r}) = \mathbf{H}_{\mathcal{R}}(\mathbf{r})\mathbf{u}^i. \tag{1}$$

$$\mathbf{u}^i = \begin{bmatrix} u_x^i & u_y^i & \omega_{xy}^i \end{bmatrix}^T, \ \mathbf{H}_{\mathcal{R}}(\mathbf{r}) = \begin{bmatrix} 1 & -\mathbf{r}_{(2)} \\ 1 & \mathbf{r}_{(1)} \end{bmatrix}. \tag{2}$$

Identifying the element velocity field enables further calculation of the velocity jumps at the interfaces, which can be implemented as in Eq. (3). Four degrees of freedom are assigned to each contact to describe the velocity discontinuities at the two nodes. These

discontinuities can be computed from the subtraction of the adjacent element velocities, with additional projection onto the local *n-s* frame (Fig. 2a).

$$\mathbf{q}_j = \left[\begin{array}{cccc} \Delta u^j_{\mathrm{n},1} & \Delta u^j_{\mathrm{t},1} & \Delta u^j_{\mathrm{n},2} & \Delta u^j_{\mathrm{t},2} \end{array}\right]^T = \left[\begin{array}{cc} -\left(\mathbf{A}^a_j\right)^T & \left(\mathbf{A}^b_j\right)^T \end{array}\right] \left[\begin{array}{c} \mathbf{u}^a \\ \mathbf{u}^b \end{array}\right]$$
$$\mathbf{A}^i_j = \left[\begin{array}{c} \mathbf{Q}_j \mathbf{H}^i_{\mathcal{R}}\left(\mathbf{r}^i_1\right) \\ \mathbf{Q}_j \mathbf{H}^i_{\mathcal{R}}\left(\mathbf{r}^i_2\right) \end{array}\right]^T,\ i = a, b,\ \mathbf{Q}_j = \left[\begin{array}{cc} \mathbf{e}^j_{\mathrm{n}} & \mathbf{e}^j_{\mathrm{t}} \end{array}\right]^T. \tag{3}$$

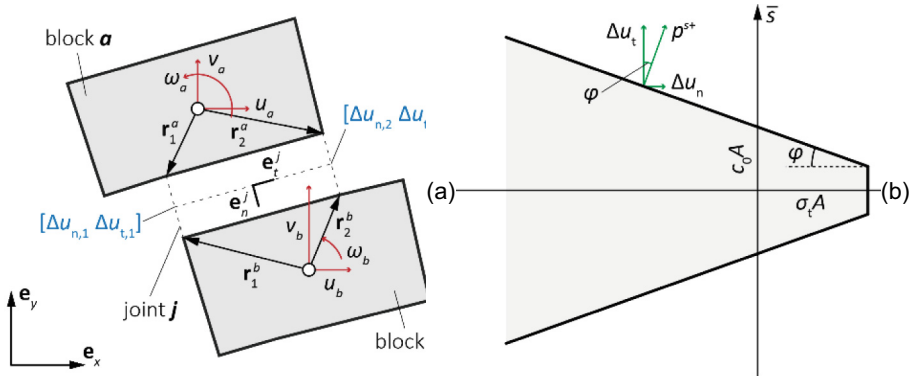

Fig. 2. 2D rigid block limit analysis: (a) computation of interfacial velocity jump; (b) interfacial constitutive model, Mohr-Coulomb friction with tension cut-off.

Assembling the relations over all the interfaces, the global constraint on element velocities and interfacial discontinuities can be written as a linear equality, known as the compatibility condition (Eq. (4)):

$$\mathbf{A}^T \mathbf{u} = \mathbf{q}. \tag{4}$$

The constitutive model for the interface is based on the 2D Mohr-Coulomb friction (Fig. 2b). Given the consideration of the tensile limit of mortar in the following FEM-based modelling, a tension cut-off is also superposed for the consistency (Eq. (5)). As a result, the matrix form of the constitutive model can be written as in Eq. (6), where the components of the constitutive operator $\mathbf{N}$ and cohesion vector $\mathbf{c}_0$ for a specific joint j have been given in Eq. (7). $\mathbf{x}$ collects the interfacial forces corresponding to the discontinuity unknowns assigned at the kinematic side.

$$\begin{aligned} F_{\mathrm{MC}}(\overline{n}, \overline{s}) &= \overline{n} \sin\varphi + |\overline{s}| \cos\varphi - \frac{1}{2} c_0 A \cos\varphi \\ F_{\mathrm{t}}(\overline{n}, \overline{s}) &= \overline{n} - \frac{1}{2}\sigma_{\mathrm{t}} A. \end{aligned} \tag{5}$$

$$\mathbf{N}\mathbf{x} - \mathbf{c}_0 = \mathbf{z}_0,\ \mathbf{z}_0 \leq 0. \tag{6}$$

$$\begin{gathered}\mathbf{N}_{j,1}=\mathbf{N}_{j,2}=\begin{bmatrix}\sin\varphi & \sin\varphi & 1\\ \cos\varphi & -\cos\varphi & 0\end{bmatrix}^{T},\ \mathbf{N}_{j}=\begin{bmatrix}\mathbf{N}_{j,1} & \\ & \mathbf{N}_{j,2}\end{bmatrix}\\ \mathbf{c}_{j,1}=\mathbf{c}_{j,2}=\frac{1}{2}\begin{bmatrix}c_0A\cos\varphi & c_0A\cos\varphi & \sigma_{\mathrm{t}}A\end{bmatrix},\ \mathbf{c}_{j}=\begin{bmatrix}\mathbf{c}_{j,1} & \mathbf{c}_{j,2}\end{bmatrix}^{T}.\end{gathered} \tag{7}$$

Assuming an associated flow rule, namely the direction of the plastic flow is always orthogonal to the constitutive limit surface, the plastic flow constraint for the kinematic side can conveniently be represented as a conjugate matrix form that associates the vector of plastic multiplier $\mathbf{p}$ and interfacial velocity jumps $\mathbf{q}$. The flow operator is the transpose of the constitutive one. The dissipation on the interfaces can be computed as an inner product of the cohesion vector and the plastic multiplier vector. More mathematical deduction can be found in the literature [12].

$$\mathbf{q}=\mathbf{N}^{T}\mathbf{p},\ \mathbf{p}\geq 0. \tag{8}$$

$$P_{D}^{\mathrm{C}}=\mathbf{c}_{0}^{T}\mathbf{p}. \tag{9}$$

If the associativity holds, the upper-bound and lower-bound LA formulations (Eqs. (10) and (11)) produce consistent predictions, which are actually a pair of dual Linear Programming (LP) problems, in terms of mathematical optimization, so that the uniqueness of the solution is guaranteed. A couple of solvers is already available and can tackle these sorts of optimizations and quickly search for the solution in a single step.

$$\begin{aligned}&\text{min. } -\mathbf{f}_{D}^{T}\mathbf{u}+\mathbf{c}_{0}^{T}\mathbf{p}\\ &\text{s.t. } \mathbf{f}_{L}^{T}\mathbf{u}=1\\ &\qquad \mathbf{A}^{T}\mathbf{u}=\mathbf{N}^{T}\mathbf{p},\ \mathbf{p}\geq 0.\end{aligned} \tag{10}$$

$$\begin{aligned}&\max\ \alpha\\ &\text{s.t. } \mathbf{A}\mathbf{x}=\alpha\mathbf{f}_{L}+\mathbf{f}_{D}\\ &\qquad \mathbf{N}\mathbf{x}-\mathbf{c}_{0}=\mathbf{z}_{0},\ \mathbf{z}_{0}\leq 0.\end{aligned} \tag{11}$$

2.2 Solution for Non-Associated Sliding

Nevertheless, the associated flow rule will bring about a spurious dilation at the interfaces, which should not be expected in a rational collapse mechanism. This assumption will even overestimate the predicted load multiplier [16]. A more realistic modeling for the interaction between bricks is the non-associated flow with zero dilation. In this case, we have to modify the plastic flow constraint by substituting the constitutive operator $\mathbf{N}$ with the flow operator $\mathbf{V}$ that constitutes the real dilation angle for the interface (Eq. (12)). The lower-bound and upper-bound formulations are therefore uncoupled, and the uniqueness of the solution is lost.

We utilise the Sequential Linear Programming (SLP) procedure, proposed by Gilbert et al. [11, 17], to search for the solution of the arch collapse with a non-associated flow rule. The iteration procedure can be expressed as sequentially solving the pair of associated problems below (Eqs. (13) and (14)), where in each iteration, the friction

angle and cohesion are updated based on the solution from the previous step. The initial solution for the iteration is taken from the associated formulation.

$$\mathbf{q} = \mathbf{V}^T\mathbf{p},\ \mathbf{p} \geq 0$$
$$\mathbf{V}_{j,1} = \mathbf{V}_{j,2} = \begin{bmatrix} \sin\psi & \sin\psi & 1 \\ \cos\psi & -\cos\psi & 0 \end{bmatrix}^T,\ \mathbf{V}_j = \begin{bmatrix} \mathbf{V}_{j,1} & \\ & \mathbf{V}_{j,2} \end{bmatrix}. \tag{12}$$

$$\begin{aligned} &\max\ \alpha_{[k]} \\ &\text{s.t.}\ \ \mathbf{A}\mathbf{x}_{[k]} = \alpha_{[k]}\mathbf{f}_L + \mathbf{f}_D \\ &\qquad \mathbf{N}_{[k]}\mathbf{x}_{[k]} - \mathbf{c}_{[k]} = \mathbf{z}_{[k]},\ \mathbf{z}_{[k]} \leq 0. \end{aligned} \tag{13}$$

$$\begin{aligned} &\text{min.}\ -\mathbf{f}_D^T\mathbf{u}_{[k]} + \mathbf{c}_{[k]}^T\mathbf{p}_{[k]} \\ &\text{s.t.}\ \ \mathbf{f}_L^T\mathbf{u}_{[k]} = 1 \\ &\qquad \mathbf{A}^T\mathbf{u}_{[k]} = \mathbf{N}_{[k]}^T\mathbf{p}_{[k]},\ \mathbf{p}_{[k]} \geq 0 \end{aligned} \tag{14}$$

At every iteration the friction angle is updated in the constitutive (flow) operator $\mathbf{N}$ through $\xi_{[k]}$ (Eqs. (15) and (16)), which is a monotonically decreasing parameter bounded by $\xi_{\min}$. This sequence gradually brings the friction angle to the dilation angle so that the real dilation of the interface can be reproduced. When ψ is equal to zero, the sliding dilation thereby vanishes in the converged solution. Remark that approaching the target dilation angle starts from the negative side to guarantee the conservative property of the searched multiplier. The interfacial cohesion is accordingly adjusted, aligned with the decrease of the frictional angle (Eq. (17)).

$$\mathbf{N}_{j,1}^{[k]} = \mathbf{N}_{j,2}^{[k]} = \begin{bmatrix} \sin\varphi_{[k]} & \sin\varphi_{[k]} & 1 \\ \cos\varphi_{[k]} & -\cos\varphi_{[k]} & 0 \end{bmatrix}^T,\ \mathbf{N}_j^{[k]} = \begin{bmatrix} \mathbf{N}_{j,1}^{[k]} & \\ & \mathbf{N}_{j,1}^{[k]} \end{bmatrix} \tag{15}$$

$$\tan\varphi_{[k]} = -\xi_{[k]}\tan\varphi + \left(1 + \xi_{[k]}\right)\tan\psi,\ \xi_{[k]} \leftarrow \max\left\{\frac{\xi_{[k-1]}}{2}, \xi_{\min}\right\} \tag{16}$$

$$\mathbf{c}_{[k]} = c_* + \mathbf{c}_0 - \left(1 + \xi_{[k]}\right)(\mathbf{N} - \mathbf{V})\mathbf{x}_{[k-1]} \tag{17}$$

Figure 3 illustrates in a more intuitive manner the physical meaning of these updates in each iteration. Actually, the updated constitutive (flow) operator and cohesion vector construct for each interface a new limit surface that passes the joint force state obtained from the previous step. These interfacial resultants are then pulled back onto the original Mohr-Coulomb limit surface, implicitly obeying the constitutive model. Consequently, the solution of the kinematic formulation will present a precise interfacial separation defined by the dilation angle when ξ decreases, whereas the Mohr-Coulomb frictional condition still holds on the static side.

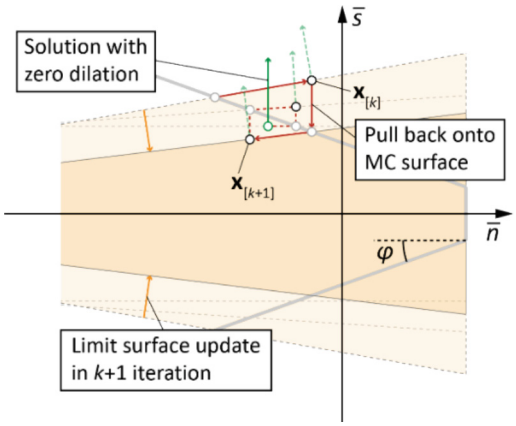

Fig. 3. Adjustment of the limit surfaces during the SLP iterations, zero-dilation case.

To improve convergence, the procedure also features a stabilisation technique to avoid the underlying fluctuation of the normal resultants at some joint nodes (Eq. (18)). The resultant solutions used to construct the new limit surface are the average of the solutions predicted in the present and the previous steps, proportioned by a suitable parameter β. A spurious cohesion term c_* is additionally inserted into the cohesion update (Eq. (17)) at the initial stage to suppress the instability that is more likely to appear in the cohesionless case. The procedure will quit when the error of the two sequential multipliers predicted reaches an assigned limit.

$$\mathbf{x}_s = \beta \mathbf{x}_{[k]} + (1 - \beta)\mathbf{x}_{[k-1]} \tag{18}$$

3 Finite Element Analysis with Ruled Explicit Meshing (REM)

In this section, the arch is modelled according to the Elastic Body and Spring Method (EBSM), developed by three of the authors for masonry structures [18]. Hyperelastic blocks (plate elements in this 2D case) are joined by special unidimensional elements available in the Strand7® library, namely Point Contacts (PC). In this case, tension PC have been used to simulate the behaviour of unilateral frictional contact. They behave as nonlinear trusses with infinite compressive and limited tensile strength. Further details are provided in the following subsection. (§3.1).

To speed up the analysis and make it easily repeatable minimising user errors, the mesh preparation is automated by a MATLAB® routine (REM) created and recently updated by some of the authors [14, 15]. By inputting a few mechanical parameters (listed in Table 1), the code prepares the data and saves a *.txt file.

Table 1. Mechanical parameters set for the REM + FEM analysis.

Property	u.m	Value
ρ	[kN/m^2]	18
E_{blocks}	[MPa]	1500
E_{joint}	[MPa]	500
f_t	[MPa]	0.05
f_c	[MPa]	∞

The file, read by Strand7, gives the data for producing the mesh of Fig. 1, a portion of which is detailed in Fig. 4, with a scheme for PC elements [19].

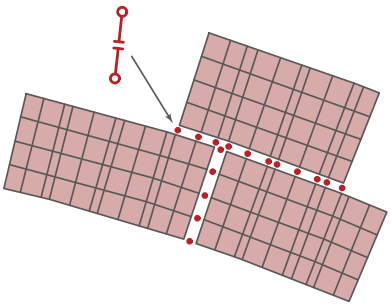

Fig. 4. Zoom of the highlighted bricks of Fig. 1. The reader can see how the mesh is formed to comply with the joint size and a visual representation of the Point Contact elements.

3.1 Point Contact Elements in Strand7

Point Contact (PC) elements connect pairs of nodes to represent interfaces. They become active or inactive depending on the relative axial displacement between the faces of objects (bricks) in contact. Therefore, this type of element is inherently nonlinear.

Three distinct interaction states are possible: the nodes may be separating (open state), approaching or in full contact without relative sliding (closed state), or in contact with mutual sliding (sliding state).

Among the four formulations of PC available in Strand7 [19], the present study employs the *Tension* formulation, which is always active in compression (no separation condition, $\Delta L < 0$) and transmits axial forces (F_{ax}) in tension and lateral forces ($F_{lat,i}$), according to Eq. (19), up to a defined threshold. Once the tensile force reaches the limit, the element is automatically released and ceases to contribute to the global stiffness matrix (Eq. (20)). No frictional behaviour is accounted for, and axial and lateral stiffness are equal. This makes the Tension formulation well-suited to interfaces whose tensile capacity is limited, such as lightly bonded construction joints of historical masonry

structures.

$$F_{ax} = k_{ax}\Delta L and F_{lat,i} = k_{lat,i} D_{lat,i} with k_{lat,i} = k_{ax} \tag{19}$$

$$F_{ax} = 0 and F_{lat,i} = 0 \tag{20}$$

Being k_{ax} and $k_{lat,i}$ the axial and lateral stiffness respectively, ΔL is the axial change in length and $D_{lat,i}$ the lateral relative displacement in direction $i = 1, 2$.

Table 2 proves that shear transfer is preserved only while the element remains active (there is contact); after axial failure, no residual tangential resistance is retained for the PC elements (no friction with null contact): when $F_{ax} = 0$, , then no shear force is accounted for anymore ($F_{lat,2} = 0$) [19].

Table 2. Summary of PC element behaviour in elastic phase and at failure with k_{ax} set as in Eq. (22) and $D_{lat,i}$ deduced from the FEM results.

# PC	d [mm] (@step)	F_{ax} [kN]	F_2 [kN]	state
1034 (ring joint)	10 (0)	0.0761	−0.1248	elastic
	10.9 (432)	−2.084	28.7670	elastic
	15 (540)	0	0	failed
1177 (radial joint)	10 (0)	−2.3582	0.2356	elastic
	10.9 (432)	0	0	failed
	15 (540)	0	0	failed

Only two input parameters are required for the analysis: the axial stiffness, calculated with the classic expression in Eq. (21), and the maximum tension of Eq. (22), filled with the data of Table 1.

$$k_{ax} = \frac{EA}{l} = \frac{E_{joint} \cdot A_{inf}}{th_{joint} \cdot 1000} \left[\frac{kN}{mm}\right] \tag{21}$$

$$F_{T,max} = \frac{A_{inf} \cdot f_t}{1000} [kN] \tag{22}$$

4 FEMANOLA

FEMANOLA [20, 21] is a Finite Element–based numerical methodology, implemented by two of the authors, specifically developed for the nonlinear analysis of masonry structures through a heterogeneous block–interface representation. Blocks are modelled as elastic plate elements, while interfaces (thick or thin for mortar and dry joint, respectively) are discretised with four-node isoparametric elements. A key feature of the joint formulation is that the elastic stiffness matrix is diagonal, with the normal component along the joint direction set to zero, thereby suppressing spurious normal stress transfer

across the interface. The stiffness matrix $\mathbf{D}_i$ of the ith element, assuming zero elastic stiffness in the normal joint direction, is given by:

$$\mathbf{D}_i = \begin{bmatrix} 0 & 0 & 0 \\ 0 & E_{k,i} & 0 \\ 0 & 0 & G_{k,i} \end{bmatrix} \tag{23}$$

where $E_{k,i}$ and $G_{k,i}$ the degraded elastic and shear moduli at the ith Gauss point at k^{th} load step.

The element stiffness is computed via standard Gaussian integration of four points in a local reference frame aligned with each joint, then rotated into the global system. Nonlinearity is handled through an iterative elastic scheme: at each loading increment, the stiffness of Gauss points that have exceeded their strength threshold is progressively reduced according to a return-to-limit-surface algorithm. The procedure is fully explicit; thus, it doesn't require sub-iterations for adequately small increments. Analyses are typically conducted under displacement control. A comprehensive description of FEMANOLA and the treatment of nonlinearity is described in detail in [20, 21], where the reader is referred for further details.

4.1 Constitutive Behaviour

The mechanical response of the interfaces follows a cohesive–frictional model with softening, coupling normal and shear behaviour. The joint constitutive model distinguishes three failure modes:

- *Tension*: an initial linear elastic response up to the tensile strength, followed by exponential softening governed by fracture energy.
- *Compression*: defined point-by-point to capture hardening and subsequent softening.
- *Shear*: a cohesive-frictional law couples tangential and normal stress. Peak and residual shear strengths vary linearly with the applied normal stress through a friction angle and zero-confinement strength parameters. Post-peak softening follows a linear-exponential decay toward the residual strength, with the Mode II fracture energy itself depending on the current normal stress level through a dimensionless scaling factor that varies parabolically under compression and linearly under tension.

All mechanical parameters have a direct physical interpretation and are defined through a preprocessing spreadsheet interface. The parameters used in this case are listed in Table 3.

Table 3. Mechanical parameters set for FEMANOLA.

Property	u.m	Value
ρ	[kN/m^2]	18
E_{blocks}	[MPa]	1500
E_{joint}	[MPa]	500

(*continued*)

Table 3. (*continued*)

Property	u.m	Value
G_{joint}	[MPa]	250
f_t	[MPa]	0.05
f_c	[MPa]	10

5 Structural Analysis

5.1 Heterogeneous LA

In the LA model, only the arrangement of brick units is considered, whereas the thickness of the mortar joints is collapsed into a zero-thickness interface. The dimension of the units is therefore correspondingly expanded to take over the space of the mortar thickness. The geometric model of the arch is sketched in AutoCAD® and then imported into MATLAB for limit analysis computation.

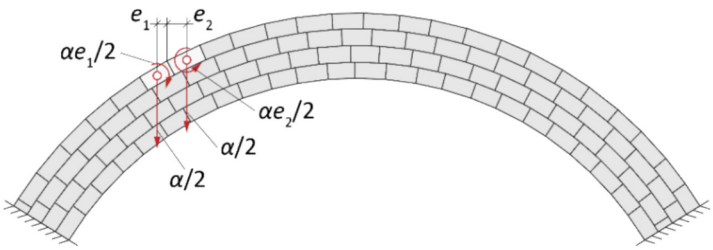

Fig. 5. Limit analysis of the main arch of the Treponti Bridge: geometry, load, and boundary conditions.

Table 4. Mechanical parameter set for the heterogeneous LA.

Parameter	u.m	Value
ρ	[kN/m^3]	18
c	[MPa]	0.05
φ	[°]	30

Table 5. Parameter setting for the non-associated procedure.

Parameter	Value
ξ_0	0.3
$\xi_{\min}$	10^{-6}
β	0.6
tol	10^{-3}
$c*$	$10^{-6}\max(\mathbf{x}_{[0]})$

As displayed in Fig. 5, the concentrated load is equivalently imposed onto two neighbouring blocks. The boundary conditions at the springing are all cohesive-frictional contact, in line with the feature of the mortar interfaces. The Limit Analysis (LA) considers interfacial modelling of both the associated flow rule and the non-associated flow rule with zero dilation (i.e., $\psi = 0$). The material properties of the brick units and the interfaces are listed in Table 4. Table 5 lists the additional parameters that are required to control the SLP procedure when considering the non-associated sliding, which follows the ones employed in [11].

The collapse results predicted from the associated formulation are illustrated in Fig. 6. The mechanism presents virtually a 4-hinge collapse, which is a typical 2D collapse of a bridge arch (see [22]). Two extrados hinges are exhibited at the loading point and right springing, whereas one intrados hinge takes place near the left springer of the arch. The intrados hinge at the right quarter span is not significant, which is smeared by the separation or sliding movement among the bricks in this domain. Unlike the thin arch collapse mechanism, a considerable sliding happens between the rings, causing a noticeable spurious dilation.

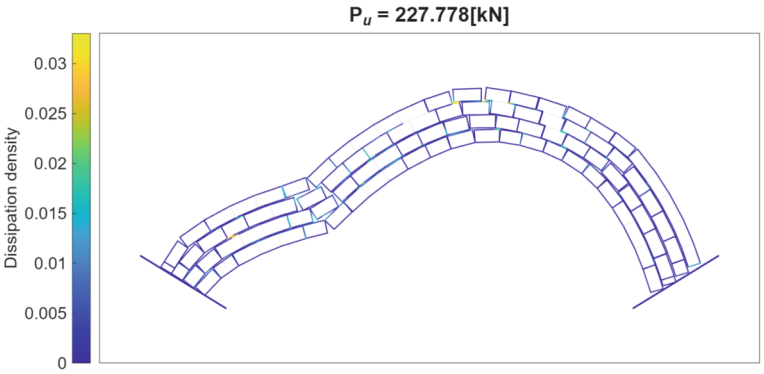

Fig. 6. Collapse of the modelled arch, limit analysis prediction with associated flow rule.

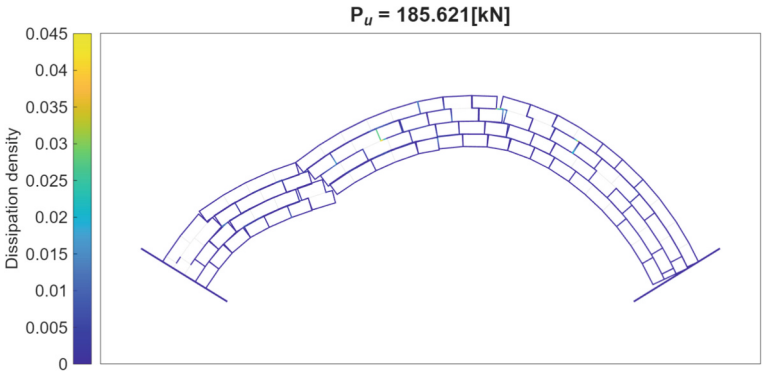

Fig. 7. Collapse of the modelled arch, limit analysis prediction with non-associated flow rule.

As expected, the non-associated formulation brings about a more conservative load prediction (Fig. 7), which is more consistent with the peak load of the FEM-based solutions. The sliding among the ring layers still appears, but the separations in normal significantly reduce, thereby exhibiting a more reasonable mechanism prediction. The presentation of the four hinges is more remarkable, in line with the indication of the FEM solutions. Due to a negative proximity to the real dilatancy on the limit surface, some penetrations take place among the brick units between the layers, although these local inaccuracies do not affect the precision of the global mechanism prediction. It should be concluded that when analysing the collapse of a thick multi-ring arch, the employment of the non-associated flow rule for the interfaces is quite necessary.

5.2 REM + FEM

The results of the arch modelled with the REM + FEM procedure are reported in Fig. 8. As can be noted, the deformed configuration at 10.9 mm displacement lines up with the ones deduced through the LA formulation. A four-hinge mechanism forms with good agreement on the location of damage.

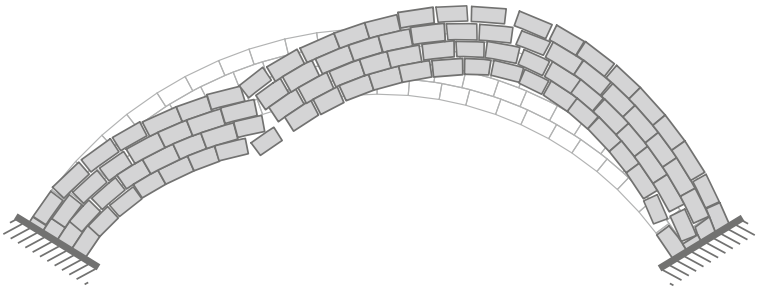

Fig. 8. Deformed configuration of the arch deduced from FEM analysis (d = 10.9 mm)

The most careful reader may note that at this stage of the analysis, one block starts detaching from the structure, initiating a mechanism that goes out of the FEM range of operability. This required the addition of some elements with a negligible elastic modulus to enhance convergence.

5.3 FEMANOLA

In this section, the results obtained by analysing the arch with FEMANOLA are gathered for two cases: one assuming infinite shear strength (Fig. 9) and the other considering finite shear strength (Fig. 10). Moreover, the output lets the user check the progressive state of damage, thus the deformed configurations are reported for the step 25 (half) and 50 (end) of the analysis.

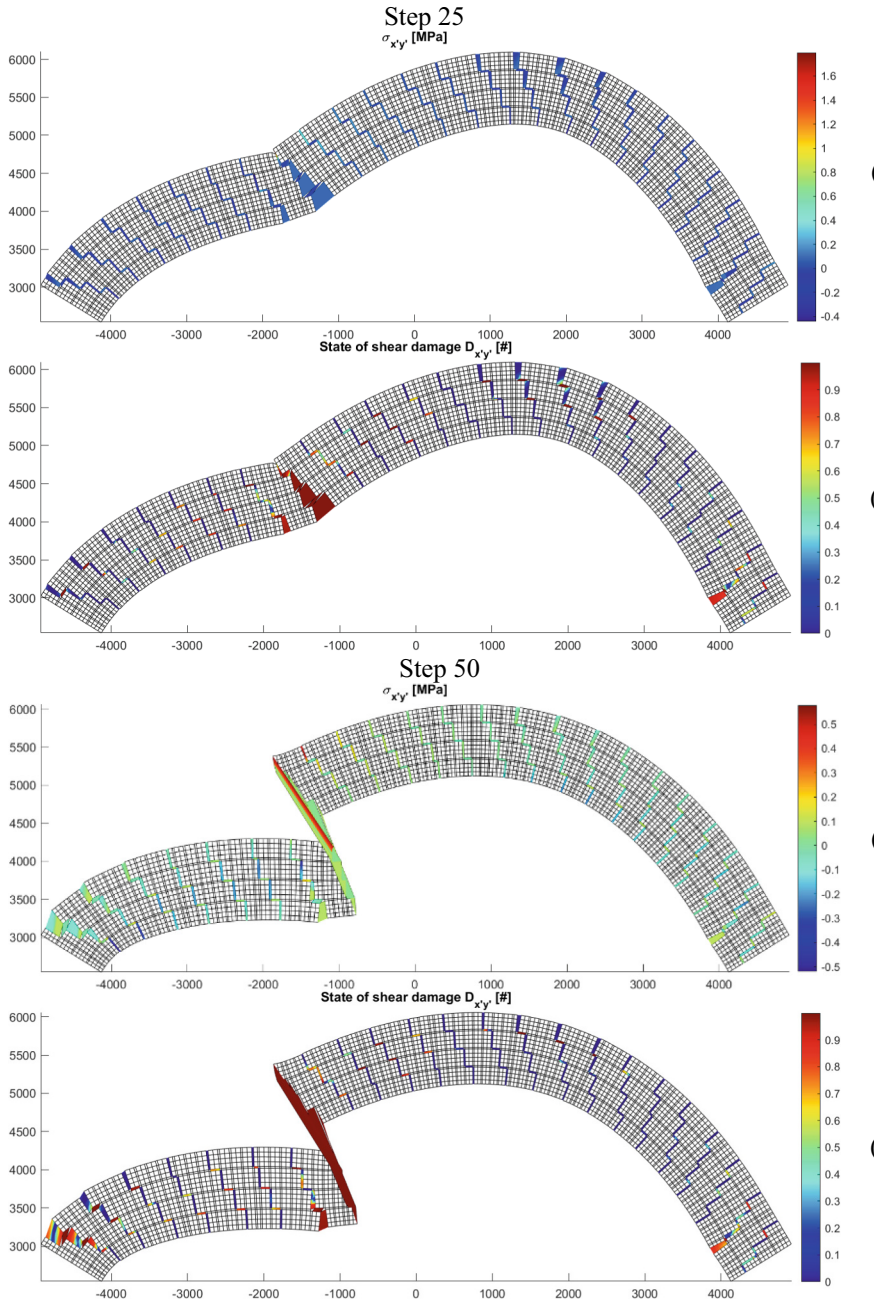

Fig. 9. Stress (a, c) and damage (b, d) states for steps 25 and 50 of FEMANOLA under the associated flow rule.

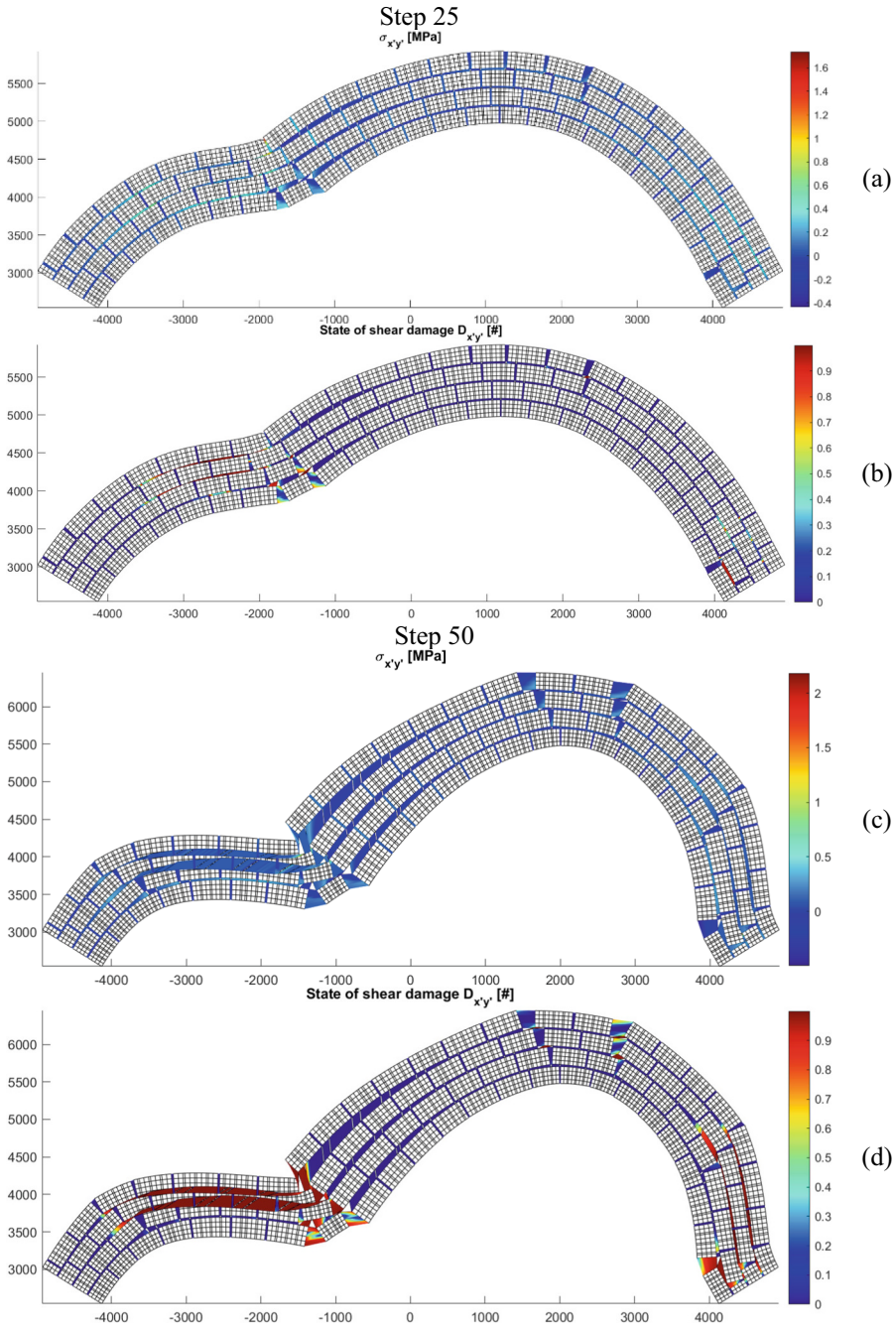

Fig. 10. Stress (a, c) and damage (b, d) states for steps 25 and 50 of FEMANOLA under the non-associated flow rule.

6 Discussion

The chart in Fig. 11 compares the capacities obtained with the three methodologies reported. The results are very satisfactory, with a good mutual agreement among them. Concerning the associated flow rule result, it indicates an underlying overestimation of the load prediction with reference to the FEM solutions. Indeed, both the predictions from the proposed REM + FEM and FEMANOLA are more conservative.

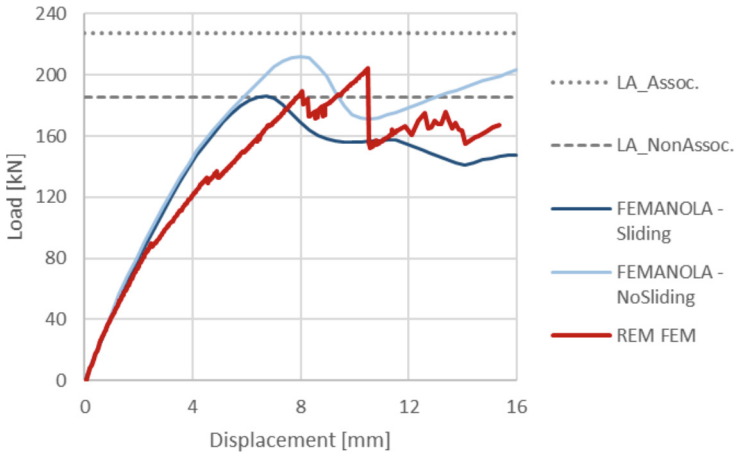

Fig. 11. Heterogeneous LA, REM + FEM, and FEMANOLA collapse load results in comparison.

The REM + FEM procedure proved to be in between the other two methods, giving more conservative results than LA while being conceptually simpler than FEMANOLA. Because of what is stated in §3.1, while the shear component is accounted in the elastic phase of interface Point Contact elements, no shear resistance is ensured after the element reaches its axial elastic limit. This may explain why the capacity curve lies between the two FEMANOLA curves of infinite and finite shear strength.

Eventually, to prove the efficiency of these analyses, Table 6 gathers some information on the time needed to run the analysis depending on the machines exploited.

Table 6. Comparison between the three methodologies and analysis time based on software environment and hardware capacity.

	U. Load [kN]	Sw. Used	Time [min]	Processor	Base freq. [GHz]
Non-associated LA	185.62	MATLAB®	< 0.03	Intel Core Ultra 9 275HX	2.70
REM + FEM	167.28	Strand7®	~ 38	Intel Core i9-14900KF	3.20
FEMANOLA	147.59	MATLAB®	~ 4	Apple M3 Max	4.05 (P-cores)

From the engineering point of view, heterogeneous Limit Analysis is particularly suitable for rapid screening of the ultimate capacity and – with non-associated flow rule – the collapse mechanisms. FEMANOLA is preferable when a detailed progressive evolution of local damage and interface stresses is of primary interest. The REM + FEM workflow provides an intermediate solution, useful when models must be generated efficiently and analysed within commercial FE environments, which are economically and theoretically more accessible.

Acknowledgments. The work has been partially carried out within the MAECI-TUBITAK Bilateral Cooperation Project 2026–2028 "ENFCorMas" Seismic Corner Collapse Mechanisms in Masonry Structures through Experimental, Numerical, and Field Studies across Italy and Turkey: From Lab to Field (Italian PI: Prof. Gabriele Milani). The Italian Ministry for Foreign affairs is gratefully acknowledged. Furthermore, the study was partially developed within the research activities carried out in the framework agreement 2024–2028 of ReLUIS Project – WP10 masonry structures (Coordinator – Prof. Guido Magenes), specifically by means of the research carried out in Task 1.1 local mechanisms and Task 2 complex systems (Task Coordinators – respectively Prof. Serena Cattari-and Prof. Sergio Lagomarsino with Dr. Gabriele Guerrini), and ReLUIS is gratefully acknowledged.

Disclosure of Interests. The authors have no competing interests to declare that are relevant to the content of this article.

References

1. Pingaro, N., Buzzetti, M., Gandolfi, A.: A numerical strategy to assess the stability of curved masonry structures using a simple nonlinear truss model. Buildings **15**, 226 (2025). https://doi.org/10.3390/buildings15132226
2. Meloni, G., Pourfouladi, M., Pingaro, N.: Parametric modelling and nonlinear FE analysis of trepponti bridge subjected to differential settlements. Buildings **16**, 47 (2025). https://doi.org/10.3390/BUILDINGS16010047
3. Nela, B., Pingaro, M., Trovalusci, P., Pasca, M.: Limit analysis of multi-ring masonry arches: a parametric study on the effects of friction angle, geometry, interlocking, and ring number. Front. Built. Environ. **9**, 1309696 (2023). https://doi.org/10.3389/fbuil.2023.1309696
4. Paris, V., Olivieri, C., Adriaenssens, S.: The impact of construction on the structural design of a complex masonry curved shell. Int. J. Space Struct. **40**, 180–194 (2025). https://doi.org/10.1177/09560599251381901;PAGEGROUP:STRING:PUBLICATION
5. Paris, V., Gobbin, F., Nannei, V.M., et al.: Distinct element method analyses for damage assessment: the northern spur of valverde bulwark in the venetian fortress of bergamo. Int. J. Arch. Heritage **19**, 687–701 (2025). https://doi.org/10.1080/15583058.2024.2345701
6. Iannuzzo, A., Block, P., Angelillo, M., Gesualdo, A.: A continuous energy-based numerical approach to predict fracture mechanisms in masonry structures: CDF method. Comput. Struct. **257**, 106645 (2021). https://doi.org/10.1016/J.COMPSTRUC.2021.106645
7. Gilbert, M., Melbourne, C.: Analysis of multi-ring brickwork arch bridges (1995)
8. Galassi, S.: An alternative approach for limit analysis of masonry arches on moving supports in finite small displacements. Eng. Fail. Anal. **145**, 107004 (2023). https://doi.org/10.1016/J.ENGFAILANAL.2022.107004
9. Galassi, S., Zampieri, P.: A new automatic procedure for nonlinear analysis of masonry arches subjected to large support movements. Eng. Struct. **276**, 115359 (2023). https://doi.org/10.1016/J.ENGSTRUCT.2022.115359

10. Galassi, S., Tempesta, G.: Safety assessment of masonry undamaged and damaged arches subjected to gravitational loads and horizontal forces: a numeric procedure to identify the optimal thrust line. Int. J. Solids Struct. **301**, 112943 (2024). https://doi.org/10.1016/J.IJSOLSTR.2024.112943
11. Gilbert, M., Casapulla, C., Ahmed, H.M.: Limit analysis of masonry block structures with non-associative frictional joints using linear programming. Comput. Struct. **84**, 873–887 (2006). https://doi.org/10.1016/j.compstruc.2006.02.005
12. Hua, Y., Milani, G.: Rigid block limit analysis of masonry arches with associated and non-associated slides. In: Research for Development. Springer Science and Business Media Deutschland GmbH, pp. 169–203 (2022)
13. Iannuzzo, A., Montanino, A.: A limit analysis-based CASS approach for the in-plane seismic capacity of masonry façades. Int. J. Solids Struct. **289**, 112633 (2024). https://doi.org/10.1016/J.IJSOLSTR.2023.112633
14. Buzzetti, M., Gandolfi, A., Pingaro, N., Milani, G.: A new advanced and simple procedure for the nonlinear static analysis of curved masonry structures. In: Protection of Historical Constructions: Proceedings of PROHITECH 2025, pp 176–183. Springer Nature, Naples (2025)
15. Gandolfi, A., Pingaro, N., Buzzetti, M., Milani, G.: An automatic procedure to simplify nonlinear static analysis of curved masonry structures. In: 14th International Conference on Structural Analysis of Historical Constructions, Lausanne (2025)
16. Livesley, R.K.: Limit analysis of structures formed from rigid blocks. Int. J. Numer. Methods Eng. **12**, 1853–1871 (1978). https://doi.org/10.1002/nme.1620121207
17. Nodargi, N.A., Intrigila, C., Bisegna, P.: A variational-based fixed-point algorithm for the limit analysis of dry-masonry block structures with non-associative Coulomb friction. Int. J. Mech. Sci. **161–162**, 105078 (2019). https://doi.org/10.1016/j.ijmecsci.2019.105078
18. Gandolfi, A., Pingaro, N., Milani, G.: Elastic body spring method (EBSM) for the stability analysis of the global vipassana pagoda in Mumbai, India. Buildings **15**, 653 (2025). https://doi.org/10.3390/buildings15050653
19. Strand7 Pty Ltd. Theoretical Manual. Theoretical backgrund to the Straus7 finite element analysis system (2004)
20. Pingaro, N., Milani, G.: Simple interface element equipped with thickness for the non-linear static heterogeneous analysis of masonry walls in-plane loaded: Implementation and validation. Eng. Struct. **351**, 122056 (2026). https://doi.org/10.1016/j.engstruct.2025.122056
21. Pingaro, N., Milani, G.: FEMANOLA v3.0 as a tool to predict settlement-induced cracks in masonry walls. In: Lecture Notes in Computer Science, pp 396–409. Springer Science and Business Media Deutschland GmbH (2026)
22. Hua, Y., Milani, G.: Novel block element with axial-only deformation for limit analysis of masonry arch bridges. Comput. Struct. **298**, 107361 (2024). https://doi.org/10.1016/j.compstruc.2024.107361